*B*1-*B*2 phase transition of ferropericlase at planetary interior conditions

F. Della Pia
Department of Physics, University Federico II, Monte S. Angelo, 80126 Napoli, Italy

D. Alfè
Department of Physics, University Federico II, Monte S. Angelo, 80126 Napoli, Italy;
Department of Earth Sciences, Thomas Young Center, University College London, 5 Gower Place, London WC1E 6BS, United Kingdom;
and London Centre for Nanotechnology, Thomas Young Centre,
University College London, 17-19 Gordon Street, London WC1H 0AH, United Kingdom

(Received 20 August 2021; revised 23 December 2021; accepted 24 February 2022; published 29 April 2022)

Using *ab initio* simulations based on *density functional theory*, we have analyzed the crystal structure and thermodynamic stability of $Mg_xFe_{1-x}O$ ferropericlase, showing how the *P*-*T* phase diagram associated with the *B*1-*B*2 phase transition of pure MgO is influenced by the presence of iron substitutional alloys. We find that a small concentration of Fe atoms contribute to an increase of the transition pressure at fixed temperature, extending the stability of *B*1 crystalline structure. Moreover, we find a significant nonhomogeneous distribution of the iron atoms between the two phases at low temperatures, with strong partitioning in the *B*1 phase, an interesting phenomena that could lead to important dynamic consequences. Finally, we analyze the effect of the iron impurities on the volume thermal expansion.

DOI: 10.1103/PhysRevB.105.134109

I. INTRODUCTION

The mineral ferropericlase ($Mg_xFe_{1-x}O$) is one of the most abundant elements of Earth's mantle. It is also expected to be a major component of high-density super-Earths [1]. It has been theoretically predicted [2] for a long time that the periclase (MgO), the end member of ferropericlase, transitions from the rocksalt structure (*B*1) to the caesium chloride structure (*B*2). The low-temperature transition pressure of MgO is higher than the pressure at the center of the Earth, and so it is not relevant for our planet. However, temperature or composition may reduce it to the point of being relevant for the Earth (∼136 GPa and ∼4000 K at the core-mantle boundary), and of course for super-Earth's interior conditions, where values up to 20 000 K and 10 TPa are expected [3,4]. For instance, Metsue and Tsuchiya [5] showed that the presence of Fe lowers the perovskite to post-perovskite phase transition in $MgSiO_3$, in addition to bringing a coexisting region of both phases.

Experimentally, the transition has only been directly observed recently by dynamic x-ray diffraction measurements [6], and its probable signature in laser-driven decaying [7,8] and steady shock experiments [9,10] has been evidenced.

Several numerical simulations have been performed to analyze the phase boundary associated with the solid-solid phase transition of the MgO, and a detailed review of the state-of-the-art literature can be found in Ref. [11]. There is a good agreement on the zero-temperature transition pressure, which is found to be in a relatively narrow range between 475–510 GPa. These variations can be principally ascribed to the use of different approximations for the exchange-correlation functional and different number of valence electrons in the pseudopotentials. This range significantly increases at high temperatures, and whether the anharmonic term is or is not neglected in the computation of the vibrational free energy plays a fundamental role. However, despite differences of $\sim 10^2$ GPa between different high-temperatures results, there is an overall common agreement between all the recent results: it is evident that not even the increase in temperature makes this transformation relevant inside the Earth's mantle, where the maximum pressure is about 136 GPa. The phase transition, on the other hand, certainly plays an important role in the study of super-Earths, where the pressure conditions can be about ten times greater than those in our Earth. The *B*1-*B*2 transition could influence internal structure and dynamics [3,12], orbital evolution [12], and exoplanet mass-radius relationships [3].

However, the mineral periclase is only the end member of ferropericlase $Mg_xFe_{1-x}O$ (typically with $x \sim 0.9$), whose structural, vibrational, and electronic properties have gained interest in the last few years [13–16]. The aim of our work is, therefore, to develop a model of study of the periclase phase diagram and then to show how it is modified by the substitution of magnesium atoms with iron impurities.

The paper is structured as follows. In Sec. II we describe the theoretical and numerical details of our simulations that led to the construction and computation of the free energy. In the first part of Sec. III we report our results for the *B*1-*B*2 phase transition of MgO, comparing with previous works. Then we show how the phase diagram is modified by the introduction of iron impurities. The effect of the phase transition and of the iron atoms on the volume thermal expansion

coefficient and on the wave velocities is reported in the Supplemental Material (SM) [17].

II. COMPUTATIONAL METHODOLOGY

In this section we outline the details of the *ab initio* simulations and of the other computational methods that we used to compute the phase boundary associated with the $B1$-$B2$ transition and the thermodynamics properties of MgO and $Mg_xFe_{1-x}O$.

A. Chemical equilibrium

The $B1$-$B2$ phase boundary of MgO periclase is obtained by the resolution of the thermodynamic relation

$$\mu_{B1}(P,T) = \mu_{B2}(P,T), \tag{1}$$

where $\mu_i(P,T)$ is the chemical potential in the i phase, with $i = B1, B2$. The chemical potential of a monospecie system is simply given by the Gibbs free energy per particle $\mu = G/N$, where

$$G(P,T) = F(V,T) + PV, \tag{2}$$

$F(V,T)$ being the Helmholtz free energy of the system.

$Mg_xFe_{1-x}O$ ferropericlase is a mixture of a solvent (MgO) and a solute (FeO), therefore the chemical equilibrium condition generalizes to

$$\mu^{B1}_{\mathrm{Fe}}\left(P,T,c^{B1}_{\mathrm{Fe}}\right) = \mu^{B2}_{\mathrm{Fe}}\left(P,T,c^{B2}_{\mathrm{Fe}}\right), \tag{3}$$

$$\mu^{B1}_{\mathrm{Mg}}\left(P,T,c^{B1}_{\mathrm{Fe}}\right) = \mu^{B2}_{\mathrm{Mg}}\left(P,T,c^{B2}_{\mathrm{Fe}}\right), \tag{4}$$

where c_{Fe} is the mole fraction of Fe atoms (solute), defined by $c_{\mathrm{Fe}} = \frac{N_{\mathrm{Fe}}}{N_{\mathrm{Fe}}+N_{\mathrm{Mg}}}$, and where we omit the subscript O for simplicity of notation.

These two equations impose two relations between $c^{B1}_{\mathrm{Fe}}, c^{B2}_{\mathrm{Fe}}$, and T, for any fixed pressure P. In the low-concentration limit $c_{\mathrm{Fe}} \to 0$ the solute chemical potential diverges logarithmically, and it is useful to write

$$\mu_{\mathrm{Fe}}(P,T,c_{\mathrm{Fe}}) = k_B T \ln(c_{\mathrm{Fe}}) + \bar{\mu}_{\mathrm{Fe}}(P,T,c_{\mathrm{Fe}}), \tag{5}$$

where $\bar{\mu}(P,T,c_{\mathrm{Fe}})$ is well behaved for all c_{Fe}, and k_B is the Boltzmann constant. In an ideal solution, $\bar{\mu}_{\mathrm{Fe}}$ is independent of c_{Fe}, but in reality the interaction between solute atoms (Fe atoms) causes it to vary with c_{Fe}.

Combining Eqs. (3) and (5) we obtain

$$\frac{c^{B1}_{\mathrm{Fe}}}{c^{B2}_{\mathrm{Fe}}} = \exp\left[\left(\bar{\mu}^{B2}_{\mathrm{Fe}} - \bar{\mu}^{B1}_{\mathrm{Fe}}\right)/k_B T\right]. \tag{6}$$

To solve Eqs. (3), (4), and (6) we proceed as in Ref. [18], outlining the main points here for convenience. We are interested in the case of moderately low c_{Fe}, but we wish to take account of the variation of $\bar{\mu}_{\mathrm{Fe}}$ with c_{Fe} to lowest order. For this reason we expand $\bar{\mu}_{\mathrm{Fe}}$ as

$$\bar{\mu}_{\mathrm{Fe}}(P,T,c_{\mathrm{Fe}}) = \mu^{\dagger}_{\mathrm{Fe}}(P,T) + \lambda_{\mathrm{Fe}}(P,T)c_{\mathrm{Fe}} + O\left(c^2_{\mathrm{Fe}}\right), \tag{7}$$

and we shall systematically neglect the term $O(c^2_{\mathrm{Fe}})$. The concentration ratio then becomes

$$\frac{c^{B1}_{\mathrm{Fe}}}{c^{B2}_{\mathrm{Fe}}} = \exp\left[\left(\mu^{\dagger,B2}_{\mathrm{Fe}} - \mu^{\dagger,B1}_{\mathrm{Fe}} + \lambda^{B2}_{\mathrm{Fe}}c^{B2}_{\mathrm{Fe}} - \lambda^{B1}_{\mathrm{Fe}}c^{B1}_{\mathrm{Fe}}\right)/k_B T\right]. \tag{8}$$

To obtain an equation for the transition temperature T, we need the corresponding expansion for μ_{Mg}. Using the Gibbs-Duhem equation

$$c_{\mathrm{Mg}}d\mu_{\mathrm{Mg}} + c_{\mathrm{Fe}}d\mu_{\mathrm{Fe}} = 0, \tag{9}$$

we have

$$\mu_{\mathrm{Mg}}(P,T,c_{\mathrm{Fe}}) = \mu^0_{\mathrm{Mg}}(P,T) + \left[\lambda_{\mathrm{Fe}}(P,T) + k_B T\right]\ln(1-c_{\mathrm{Fe}}) + \lambda_{\mathrm{Fe}}(P,T)c_{\mathrm{Fe}} + O(c^2_{\mathrm{Fe}}), \tag{10}$$

where μ^0_{Mg} is the chemical potential of pure MgO, and we have used the fact that $c_{\mathrm{Mg}} = 1 - c_{\mathrm{Fe}}$. To linear order in c_{Fe}, this gives

$$\mu_{\mathrm{Mg}}(P,T,c_{\mathrm{Fe}}) = \mu^0_{\mathrm{Mg}}(P,T) - k_B T c_{\mathrm{Fe}}. \tag{11}$$

Expanding the chemical potential of pure MgO to linear order in the difference $T - T^0$, where T^0 is the transition temperature of pure MgO, we obtain

$$\mu^0_{\mathrm{Mg}}(P,T) \sim \mu^0_{\mathrm{Mg}}(P,T^0) + \left(\frac{\partial \mu^0_{\mathrm{Mg}}}{\partial T}\right)_{T=T^0}(T-T^0), \tag{12}$$

and substituting Eqs. (11) and (12) in Eq. (4) we obtain

$$-k_B T c^{B2}_{\mathrm{Fe}} + \mu^{0,B2}_{\mathrm{Mg}}\left(P,T^0\right) + \left(T-T^0\right)\left(\frac{\partial \mu^{0,B2}_{\mathrm{Mg}}}{\partial T}\right)_{T=T^0} = -k_B T c^{B1}_{\mathrm{Fe}} + \mu^{0,B1}_{\mathrm{Mg}}(P,T^0) + (T-T^0)\left(\frac{\partial \mu^{0,B1}_{\mathrm{Mg}}}{\partial T}\right)_{T=T^0}.$$

Since $\mu^{0,B1}_{\mathrm{Mg}}(P,T^0) = \mu^{0,B2}_{\mathrm{Mg}}(P,T^0)$ (by definition of T^0), and considering that $s^0_{\mathrm{Mg}} = -(\frac{\partial \mu^0_{\mathrm{Mg}}}{\partial T})_{T=T^0}$ is the entropy per formula unit of pure MgO at the transition temperature, we can rewrite the previous equation as

$$(T-T^0) = \frac{k_B T}{\Delta s^0_{\mathrm{Mg}}}\left(c^{B1}_{\mathrm{Fe}} - c^{B2}_{\mathrm{Fe}}\right), \tag{13}$$

where $\Delta s^0_{\mathrm{Mg}} = s^{0,B2}_{\mathrm{Mg}} - s^{0,B1}_{\mathrm{Mg}}$. Equations (6) and (13) must be solved self-consistently. In particular, we need to find a way to compute the chemical potential $\bar{\mu}_{\mathrm{Fe}}$, and so the functions $\mu^{\dagger}_{\mathrm{Fe}}(P,T)$ and $\lambda_{\mathrm{Fe}}(P,T)$. In a multispecie system, the chemical potential of the specie j (in our case $j = $ Mg,Fe) is the first derivative of the Gibbs free energy w.r.t. the number of particles of the specie j, i.e.,

$$G(P,T,N_{\mathrm{Mg}},N_{\mathrm{Fe}}) = N_{\mathrm{Mg}}\mu_{\mathrm{Mg}} + N_{\mathrm{Fe}}\mu_{\mathrm{Fe}}. \tag{14}$$

Indicating with $\bar{G}(P,T,N_{\mathrm{Mg}},N_{\mathrm{Fe}})$ the Gibbs free energy due to the well-behaved part of the chemical potentials, i.e.,

$$\bar{G}(P,T,N_{\mathrm{Mg}},N_{\mathrm{Fe}}) = N_{\mathrm{Mg}}\bar{\mu}_{\mathrm{Mg}} + N_{\mathrm{Fe}}\bar{\mu}_{\mathrm{Fe}}, \tag{15}$$

then we can compute $\bar{\mu}_j(P,T)$ approximating the derivative with the finite difference:

$$\bar{\mu}_{\mathrm{Fe}}(N_{\mathrm{Fe}}) - \bar{\mu}_{\mathrm{Mg}}(N_{\mathrm{Fe}}) \sim \frac{\bar{G}(N_{\mathrm{Mg}}-\delta N, N_{\mathrm{Fe}}+\delta N) - \bar{G}(N_{\mathrm{Mg}}+\delta N, N_{\mathrm{Fe}}-\delta N)}{2\delta N}. \tag{16}$$

TABLE I. Comparison between this work EOS parameters and previous results. References [27,28] are theoretical simulations based on LDA+pseudopotential technique while Ref. [2] is an all electron (LAPW) LDA calculation.

EOS	This work (electrons)	This work (electrons+ions)	LDA [27]	LDA [28]	LDA [2]	Experiment [29]
V_0 (Å^3)	19.05	19.29	19.05	18.8	18.1	18.68
K_0 (GPa)	152.2	147.4	172.6	159	172	160.2
K_0'	4.1	4.0	4.0	4.3	4.1	3.9

Computing the Gibbs free energy of $Mg_xFe_{1-x}O$ for several concentrations of the iron impurities, we can fit Eq. (7) to obtain the *ab initio* quantities $\mu^\dagger(P,T)$ and $\lambda(P,T)$.

We write the Helmholtz free energy as

$$F(V,T) = E(V) + F_{\text{vib}}(V,T), \tag{17}$$

where $E(V)$ is the static lattice contribution, i.e., the electronic zero-temperature contribution to the free energy, and $F_{\text{vib}}(V,T)$ is the vibrational contribution due to atomic motion. In this work, the vibrational contribution is generally computed in the framework of the quasiharmonic approximation (QHA), while the effects of the anharmonic contribution to the free energy are only computed in the case of MgO. For $Mg_xFe_{1-x}O$ we also include the contribution due to different possible spatial distributions of the iron atoms. We computed $F(V,T)$ at several volumes and fitted the results to a Birch Murnaghan equation of state to calculate the pressure from its analytic derivative, which allow us to obtain $\tilde{G}(P,T)$.

B. Static lattice contribution

The present results have been obtained with the use of the `VASP.4.6` [19,20] package in the framework of the projector augmented wave (PAW) method [20] and by means of the generalized gradient approximation (GGA) [21]. The PAW core radii are equal to 1.7 Å for Mg, with $2s$, $2p$, and $3s$ states as valence electrons (10 electrons), 1.52 Å for O, with $2s$ and $2p$ states as valence electrons (6 electrons), and 2.2 Å for Fe, with $3p$, $3d$, and $4s$ states as valence electrons (14 electrons).

The static lattice contribution is computed using unit cells with 2 atoms for MgO, while we used the 128 atoms supercell to investigate the effect of iron impurities in ferropericlase. The cutoff energy for the plane-wave set is 800 eV, while the global break condition for the electronic self-consistent equations is 10^{-7} eV. The Brillouin zone is sampled with a $32 \times 32 \times 32$ Monkhorst-Pack [22] mesh of $\boldsymbol{k}$ points for MgO and a $2 \times 2 \times 2$ mesh for $Mg_xFe_{1-x}O$.

Fixing several volumes V in the region 8–11 Å^3 for MgO primitive cells and 512–704 Å^3 for the $Mg_xFe_{1-x}O$ 128 atoms supercells, we computed the electronic zero-temperature contribution to the free energy $E(V)$, which is fitted to the Birch-Murnaghan equation of state (EOS) [23], given by

$$E(V) = E_0 + \frac{3}{2}V_0K_0\left[\frac{3+6\chi}{4}\left(\frac{V_0}{V}\right)^{4/3} - \frac{\chi}{2}\left(\frac{V_0}{V}\right)^2 - \frac{3+3\chi}{2}\left(\frac{V_0}{V}\right)^{2/3} + \frac{2\chi+3}{4}\right], \tag{18}$$

where E_0 is the value of the energy at the zero pressure equilibrium volume V_0, $K_0 = -V_0(\frac{dP}{dV})_{V_0}$ is the zero pressure bulk modulus, and $\chi = \frac{3}{4}(4 - K_0')$, with $K_0' = (\frac{dK}{dP})_{P=0}$.

Then, the associated pressure is obtained as $P_{\text{el}} = -\frac{\partial E}{\partial V}$.

C. Phonons and quasiharmonic approximation

The lattice contribution to the Helmholtz free energy in the framework of QHA is given by

$$F_{\text{harm}}(V,T) = \frac{k_BT}{\Omega}\int_{\text{BZ}} d\boldsymbol{q}\sum_s \ln\left[2\sinh\left(\frac{\hbar\omega_{\boldsymbol{q},s}(V)}{2k_BT}\right)\right], \tag{19}$$

where $\Omega = \frac{(2\pi)^3}{V}$ is the volume of the Brillouin zone, and $\omega_{\boldsymbol{q},s}(V)$ is the volume-dependent frequency of the sth vibrational mode of the crystal at wave-vector $\boldsymbol{q}$.

The calculation of the phonon frequencies in the QHA is performed using the *small displacement method* with the `PHON` [24] code. In the case of insulators, the long range forces make it more difficult to calculate phonons in the whole BZ using the small displacement method, mainly because the longitudinal optical frequencies are split from the transverse ones at the Γ point due to a nonanalytic term in the dynamical matrix, which is not captured. However, in the thermodynamic limit (infinite crystal) the contribution of a single vibrational mode does not influence the total free energy, and it has been shown [24] that the thermodynamic properties of MgO obtained with a supercell including 128 atoms are unaffected by the nonanalytic term in the dynamical matrix.

Forces between atoms are computed using `VASP`: the DFT calculations are performed with a 128 atoms supercell, sampling the Brillouin zone with a $4 \times 4 \times 4$ Monkhorst-Pack mesh in the case of MgO. Including iron impurities dramatically reduces the symmetry of the system, therefore numerous displacements are needed in the small displacement method. For this reason, we used only the Γ point for ferropericlase, which is a good compromise between accuracy and computational cost. In fact, tests on MgO show that using a $2 \times 2 \times 2$ or a $4 \times 4 \times 4$ $\boldsymbol{k}$ points in the computation of the forces, leads to a variation in the transition pressures of 0.1%–0.2% at low temperatures and 2%–3% for temperatures higher than ∼5000 K. An analogous result is obtained comparing transition pressures computed with the $2 \times 2 \times 2$ $\boldsymbol{k}$ points and only the Γ point in the case of $Mg_{63}Fe_1O_{64}$. For this reason we reasonably expect this approximation to not significantly influence our results.

The cutoff energy for the plane-wave set is 500 eV, while the break condition for the electronic self-consistent equation is 10^{-7} eV.

The integral over the Brillouin zone in Eq. (19) is approximated with a finite sum over a uniformly distributed $32 \times 32 \times 32$ $\boldsymbol{q}$-points grid.

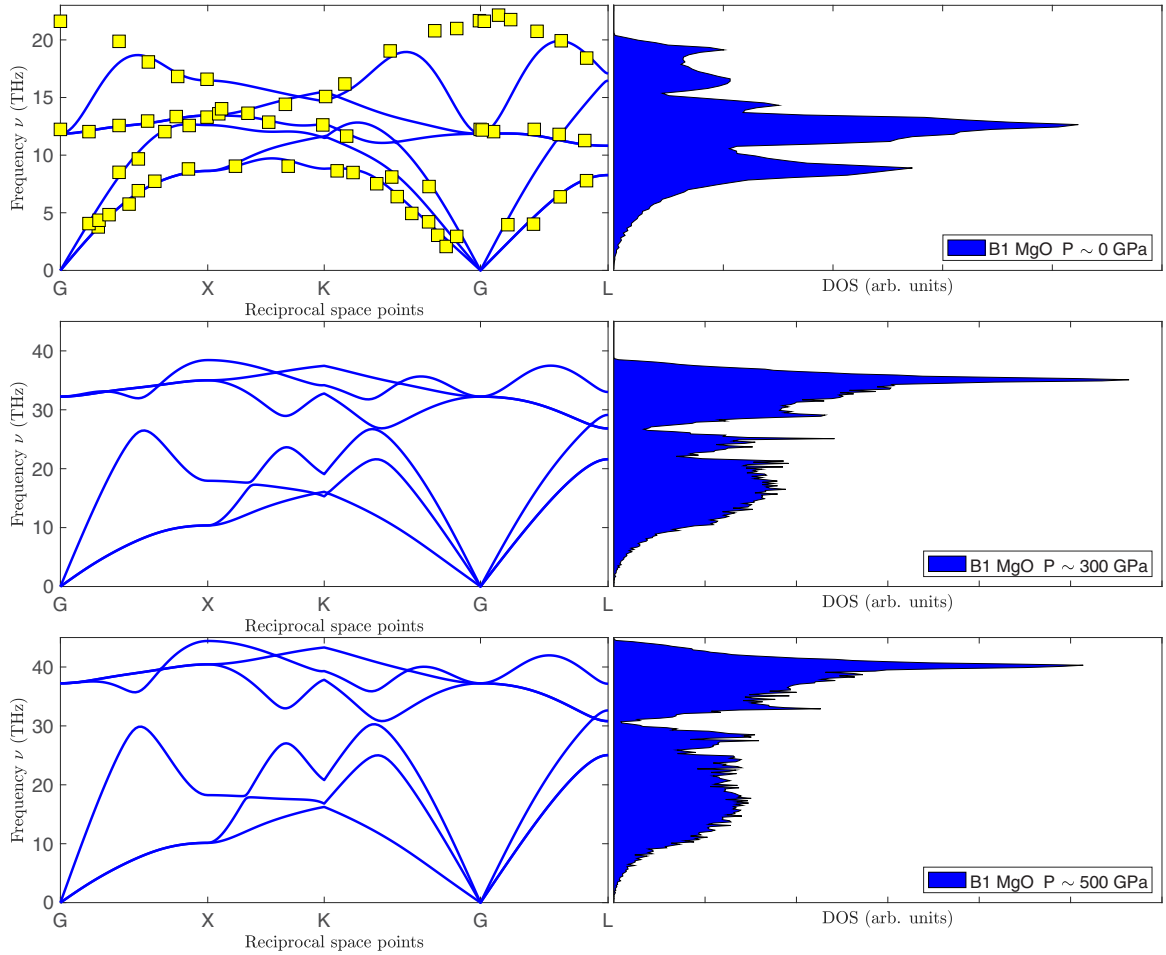

FIG. 1. Phonon dispersion curves of MgO in $B1$ crystalline structure at ∼0, 300, and 500 GPa (on the left) and the respective density of states (on the right). Experimental data (yellow squares) are taken from Refs. [30,31].

The harmonic contribution is computed for all volumes described in the previous section, spanning temperature in the range 0–1000 K with step 100 K and in the range 1000–7000 K with step 500 K. Fitting the curve $F(V,T) = E(V) + F_{\text{harm}}(V,T)$ to the EOS for every temperature T, the total pressure (in the quasiharmonic approximation) is computed as $P(T) = -\frac{\partial F}{\partial V}|_T$.

D. Anharmonicity and thermodynamic integration

At high temperature anharmonic effects in solids may start to play an important role, and the quasiharmonic approximation may not be accurate enough. To compute the full free energy of the system we use the *thermodynamic integration* procedure [25]. We write the total potential energy of the system as

$$U(\boldsymbol{R}_1,\ldots,\boldsymbol{R}_N) = U(\{\boldsymbol{R}\}) = U_{\text{harm}}(\{\boldsymbol{R}\}) + U'(\{\boldsymbol{R}\}), \quad (20)$$

where $\boldsymbol{R}_i$ is the position of ith atom, N is the number of atoms in the crystal, U_{harm} is the harmonic potential, and U' is, by definition, the error committed in approximating U with U_{harm}. Since anharmonicity is only going to be important in the high temperature limit, we can compute it assuming the classical approximation for the partition function. In this case, the anharmonic contribution to the free energy is

$$F' = F - F_{\text{harm}} = \int_0^1 d\lambda \langle U' \rangle_\lambda, \quad (21)$$

where $\langle\ \rangle_\lambda$ defines the canonical ensemble average in the ensemble with the intermediate potential energy

$$U_\lambda = (1-\lambda)U_{\text{harm}} + \lambda U. \quad (22)$$

Canonical averages are computed as time averages using trajectories generated with molecular dynamics simulations. Each MD simulation was 5000 steps long with a time step of 0.5 fs. Ergodicity is insured by coupling the system with an Andersen heat bath [26].

The anharmonic contribution to the free energy has been computed in the case of MgO considering the 128 atoms supercell. High accuracy molecular dynamics simulations, i.e., simulations with a high density $\boldsymbol{k}$ points grid, are very expensive. However, the anharmonic contribution is the smallest term in the decomposition:

$$F(V,T) = E(V) + F_{\text{harm}}(V,T) + F'(V,T), \quad (23)$$

therefore using a low density grid should give a significant error in $E(V)$ that might be less important for F_{harm}, and even less for F'. For this reason we compromised with computa-

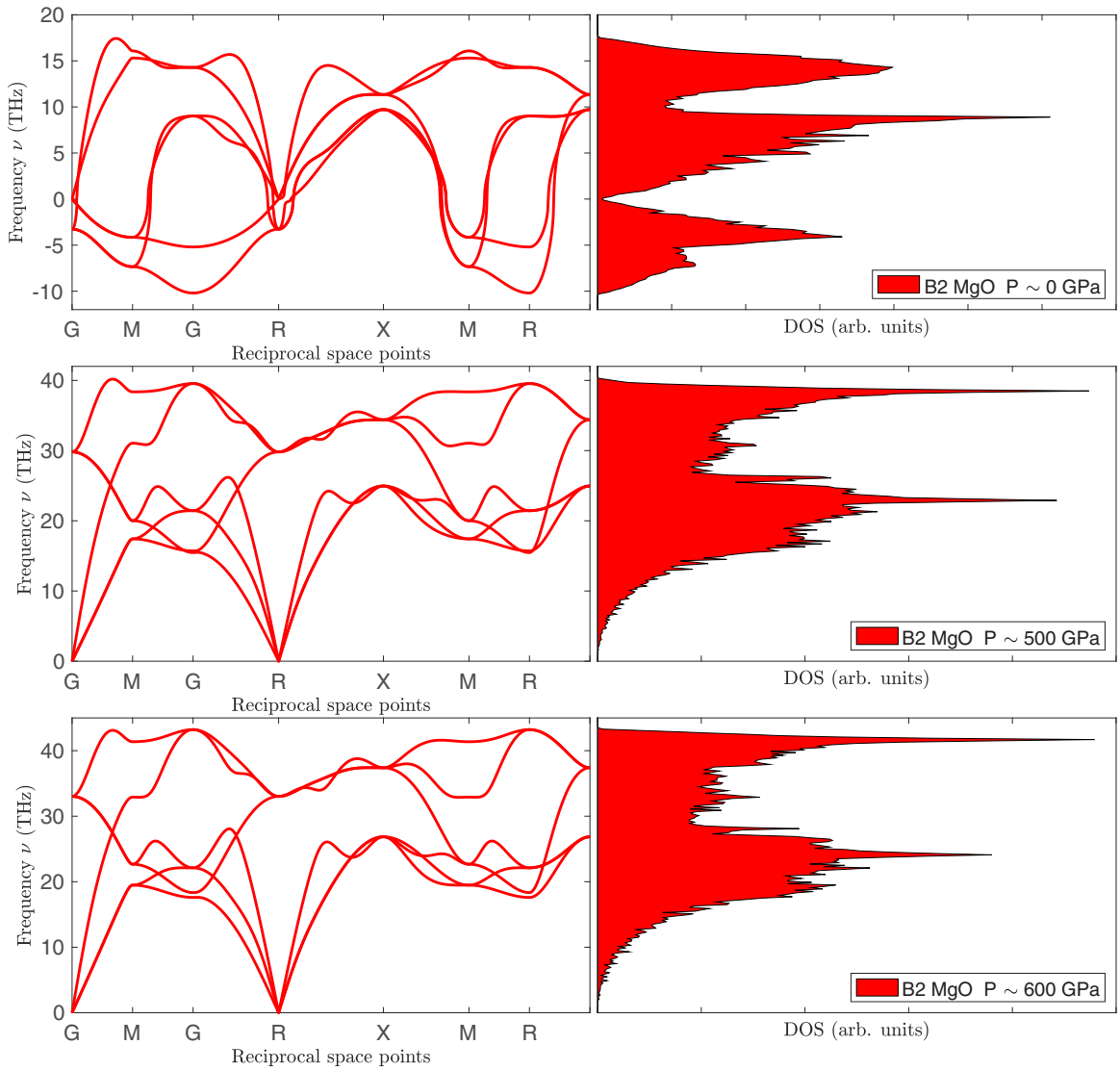

FIG. 2. Phonon dispersion curves of MgO in *B*2 crystalline structure at ∼0, 500, and 600 GPa (on the left) and the respective density of states (on the right).

tional cost and use only the Γ point in the Brillouin zone, without significantly affecting the total accuracy.

In order to verify this assumption, we used the perturbative expansion of thermodynamic integration. In detail, indicating with ΔU the difference between the energy of the system computed with a $2 \times 2 \times 2$ $\boldsymbol{k}$-points grid and using only the Γ point (for a fixed V, T configuration), i.e.,

$$\Delta U = U(2 \times 2 \times 2) - U(\Gamma), \tag{24}$$

then is easy to show that the difference in the respective free energies can be approximated as

$$\Delta F = F(2 \times 2 \times 2) - F(\Gamma) \sim \langle \Delta U \rangle_{\lambda=0} - \frac{1}{2k_B T}\left[\langle \Delta U^2 \rangle_{\lambda=0} - \langle \Delta U \rangle^2_{\lambda=0}\right], \tag{25}$$

where the intermediate potential is

$$U_\lambda = (1-\lambda)U_1 + \lambda U_2. \tag{26}$$

Computing independently, the quantities

$$\Delta U_0 = U_0(2 \times 2 \times 2) - U_0(\Gamma),$$
$$\Delta F_{\text{harm}} = F_{\text{harm}}(2 \times 2 \times 2) - F_{\text{harm}}(\Gamma),$$

we used the perturbative expansion method to estimate the effect of the $2 \times 2 \times 2$ $\boldsymbol{k}$-points grid on the anharmonic corrections as

$$\Delta F' = F'(2 \times 2 \times 2) - F'(\Gamma) = \Delta F - \Delta U_0 - \Delta F_{\text{harm}}. \tag{27}$$

E. Spatial distribution of iron impurities and the free energy of mixing

We analyzed the thermodynamics stability of the $Mg_xFe_{1-x}O$ ferropericlase by gradually substituting one Mg atom with one Fe atom in the 128 atoms supercell. Once the number of impurities is greater than one, it is necessary to study also the spatial distribution of the iron atoms. In fact, due to the translational invariance, the analysis of $Mg_{63}Fe_1O$

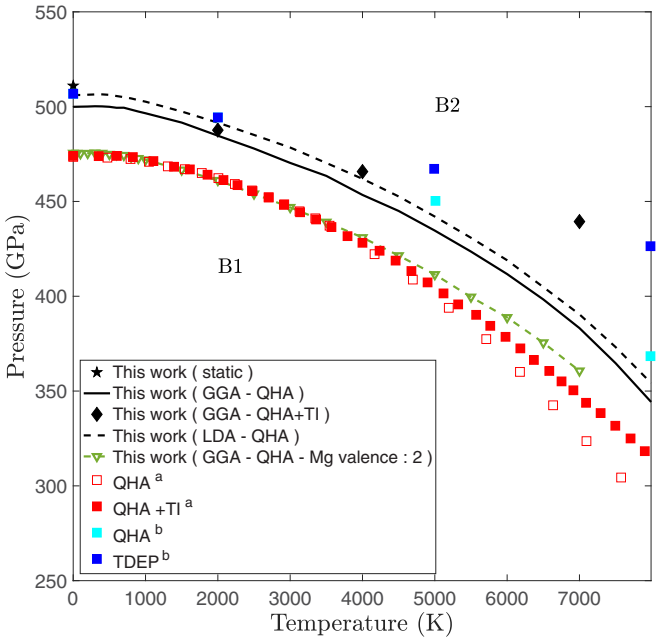

FIG. 3. Phase diagram of periclase. [a]Ref. [9]. [b]Ref. [11]. The small difference between our GGA result (black solid line) and Ref. [11] is due to the different type of exchange-correlation functional, as showed by our LDA result (black dashed line).

is independent of the position of the impurity: we can fix it in 64 different ways that are all equivalent. By contrast, when the number of impurities is $n > 1$, we can consider $\binom{64}{n}$ different configurations (not all independent), which give different contributions to the free energy of the system. This configurational contribution has been studied using again the technique of the thermodynamic integration, coupled with a Monte Carlo algorithm to explore the configurations space of the canonical ensemble. Indicating with c_k all the possible configurations, with $k = 1, \ldots, \binom{64}{n}$, and with c_* the configuration corresponding to the minimum of the free energy (for a fixed V, T), then the Helmholtz free energy can be written as

$$F(V,T) = E_{c_*}(V) + F_{\text{harm},c_*}(V,T) + F_{\text{conf}}(V,T), \tag{28}$$

where E_{c_*} and F_{harm,c_*} are, respectively, the electronic ground state and ions harmonic contribution in the configuration c_*, while the term F_{conf} is the additional contribution due to the possible spatial distribution which needs to be computed. The term F_{conf}, which is the so-called *excess free energy of mixing*, is computed using thermodynamic integration as

$$F_{\text{conf}}(V,T) = \int_0^1 d\lambda \langle U_{\text{mix}} \rangle_\lambda, \tag{29}$$

where U_{mix} is the iron atoms interaction energy in the different configurations, that is $U_{\text{mix}}(c_*) = 0$ and

$$U_{\text{mix}}(c_k) = E_{c_k} + F_{\text{harm},c_k} - E_{c_*} - F_{\text{harm},c_*}. \tag{30}$$

The canonical ensemble averages are computed in the system with potential energy $U_\lambda = \lambda U_{\text{mix}}$, which is sampled, in each simulation (that is fixed V, T, and λ), using the Metropolis algorithm with 10^7 steps among the total configurations. This procedure is repeated for $\lambda = 0, 0.1, \ldots, 1.0$, and then we computed the integral in Eq. (29) by numerical methods.

III. RESULTS AND DISCUSSION

The methods described in the previous section were used to compute the landscape of the Helmholtz and Gibbs free energy of the minerals periclase and ferropericlase, investigating the region from 100 to 1000 GPa and from 0 to 7000 K, which are relevant for the interior of Earth and super-Earths.

A. Thermodynamics of MgO

1. Equation of state

The equation of state parameters are first computed for MgO in the $B1$ crystalline structure fitting the electronic ground state contribution $E(V)$ to the Birch-Murnaghan EOS [Eq. (18)]. Subsequently, using the phonon frequencies we computed the zero-temperature ionic contribution to the free energy, i.e., the *zero-point energy* given by

$$F_{\text{harm}}(V,0) = \frac{1}{\Omega}\int_{\text{BZ}} d\boldsymbol{q} \frac{\hbar\omega_{\boldsymbol{q},s}(V)}{2}, \tag{31}$$

therefore we computed the corrections to the EOS parameters due to the lattice contribution. The obtained results are reported in Table I, together with both previous theoretical (static lattice) results and experimental data (obtained at $P = 0$ and $T = 300$ K).

2. Vibrating lattice

Figure 1 shows the phonon dispersion curves of MgO in the $B1$ crystalline structure at ∼0, 300, and 500 GPa. In the first case experimental data are also displayed, taken from Refs. [30,31].

The difference between the frequencies at Γ is due to the fact that the LO frequency at Γ is wrongly described as degenerate with the two TO frequencies, and therefore the Fourier interpolation of the frequencies is wrong. As mentioned above, this has no effect on the accuracy of the computed free energy of the crystal.

The first two cases are still within the stability field of the $B1$ structure, while the latter one is in the region of the phase transition. At all these pressures, the structure remains dynamically stable, the phonon spectrum extends to higher frequencies, acquires a more complicated structure, and a pseudogap develops in the middle of the spectrum.

Figure 2 shows the phonon dispersion curves of MgO in the $B2$ crystalline structure at ∼0, 500, and 600 GPa. The first case is in the stability field of the $B1$ structure, 500 GPa is in the region of the phase transition, while 600 GPa is in the stability field of the $B2$ structure. This phase is dynamically unstable at 0 GPa, and has whole soft phonon branches (negative frequencies representing imaginary values). However, it becomes dynamically stable above ∼110 GPa.

3. Anharmonicity

We computed the anharmonic corrections at 2000, 4000, and 7000 K for the analyzed volumes. The anharmonic term is $F' \sim 10^{-3}$ eV at 2000 K for both crystalline structures, corresponding to a correction of ∼1% to F_{harm}, while it becomes $F' \sim 10^{-1}$ eV at 7000 K, corresponding to a correction of ∼10% to F_{harm}.

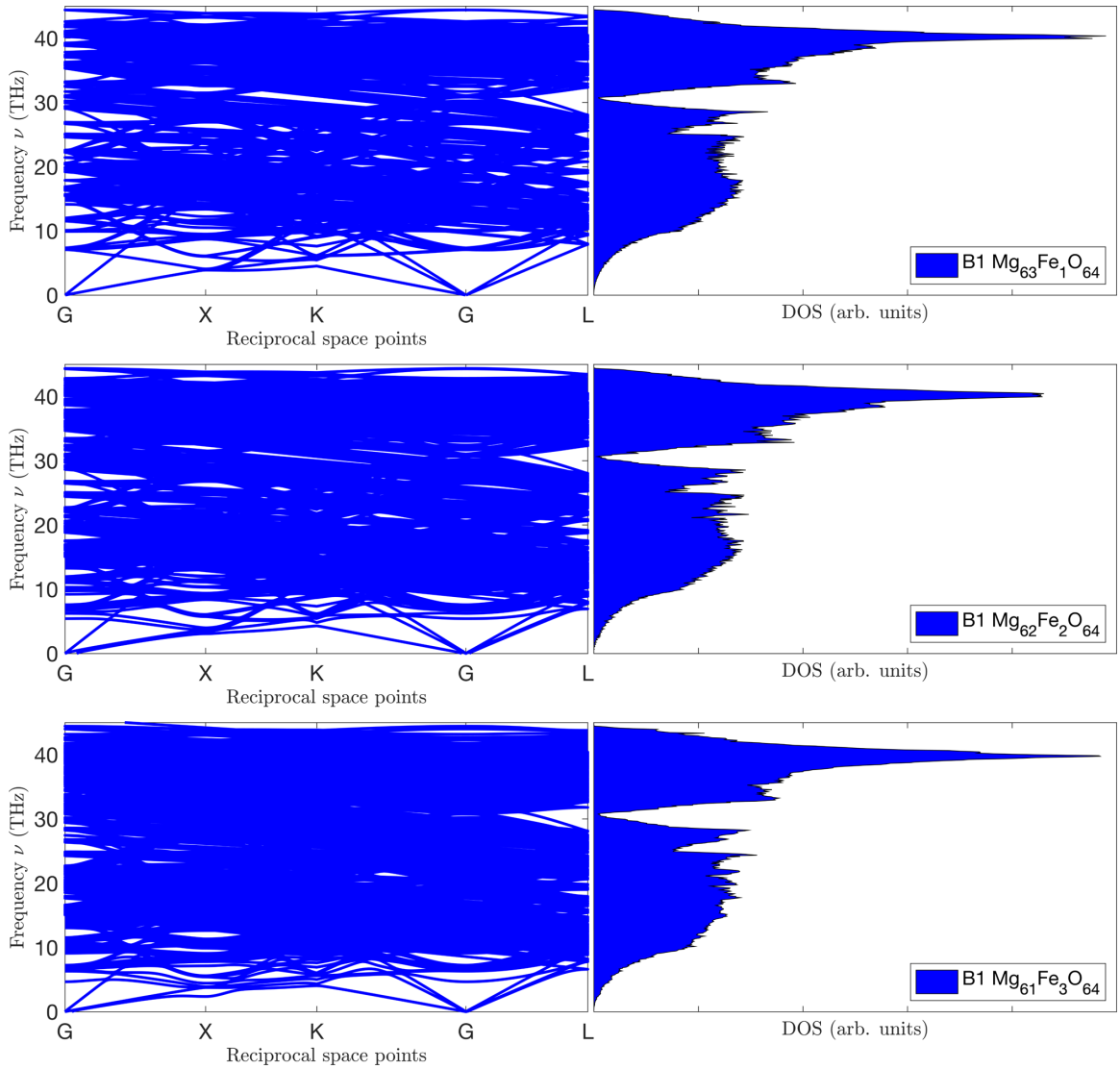

FIG. 4. Phonon dispersion of $Mg_{63}Fe_1O_{64}$, $Mg_{62}Fe_2O_{64}$, and $Mg_{61}Fe_3O_{64}$ in the $B1$ crystalline structure at ∼500 GPa.

As described in Sec. II D we used the perturbative expansion method to estimate the difference in the anharmonic correction due to the use of a $2 \times 2 \times 2$ $\boldsymbol{k}$-points grid. In detail, we computed the anharmonic contribution at 9.0 and 10 Å^3 for both crystalline structures at $T = 2000$ and 7000 K, finding that using only the Γ point leads to a slight underestimation of the anharmonic contribution. However, we find that using the higher-density grid, the quantity $F'_{B1} - F'_{B2}$, i.e., the anharmonic term influencing the variation in the transition pressure, changes only of ∼4% at $T = 2000$ K, and ∼20%-30% at $T = 7000$ K, therefore the use of only the Γ point in the computation of F' does not influence significantly the accuracy of our results.

4. B1-B2 phase transition

Resolving Eq. (1) with numerical methods we obtained the phase diagram associated with the solid-solid phase transition, reported in Fig. 3 together with previous recent results. In particular, we also report our results for the transition curve in the framework of local density approximation (LDA), showing that the choice of the exchange-correlation functional (between LDA and GGA) does not significantly affect the transition pressure. It is also reported the static transition pressure, i.e., the zero-temperature transition pressure obtained without taking into account the zero-point energy. In particular, the zero-temperature lattice contribution is responsible for a diminution of ∼15 GPa of the static transition pressure.

Moreover, we have verified that the difference between our curves (GGA or LDA) and the transition curve from Ref. [9], (or other previous results, e.g., Ref. [27]) is due to the choice of valence electrons in the Mg pseudopotential. In fact, Fig. 3 also shows our result (GGA) obtained considering only 2 valence electrons ($3s^2$) in the Mg pseudopotential, which is in very good agreement with Ref. [9]. The significant difference between the curves with different valence electrons (∼30 GPa) means that at these high pressures there is an important response of $2s$ and $2p$ electrons that cannot be neglected for an high-accuracy description of Mg.

Finally, we notice that even the small contribution of the anharmonic term at 2000 K defines an observable variation (∼1%) of the transition pressure. It is really clear that the

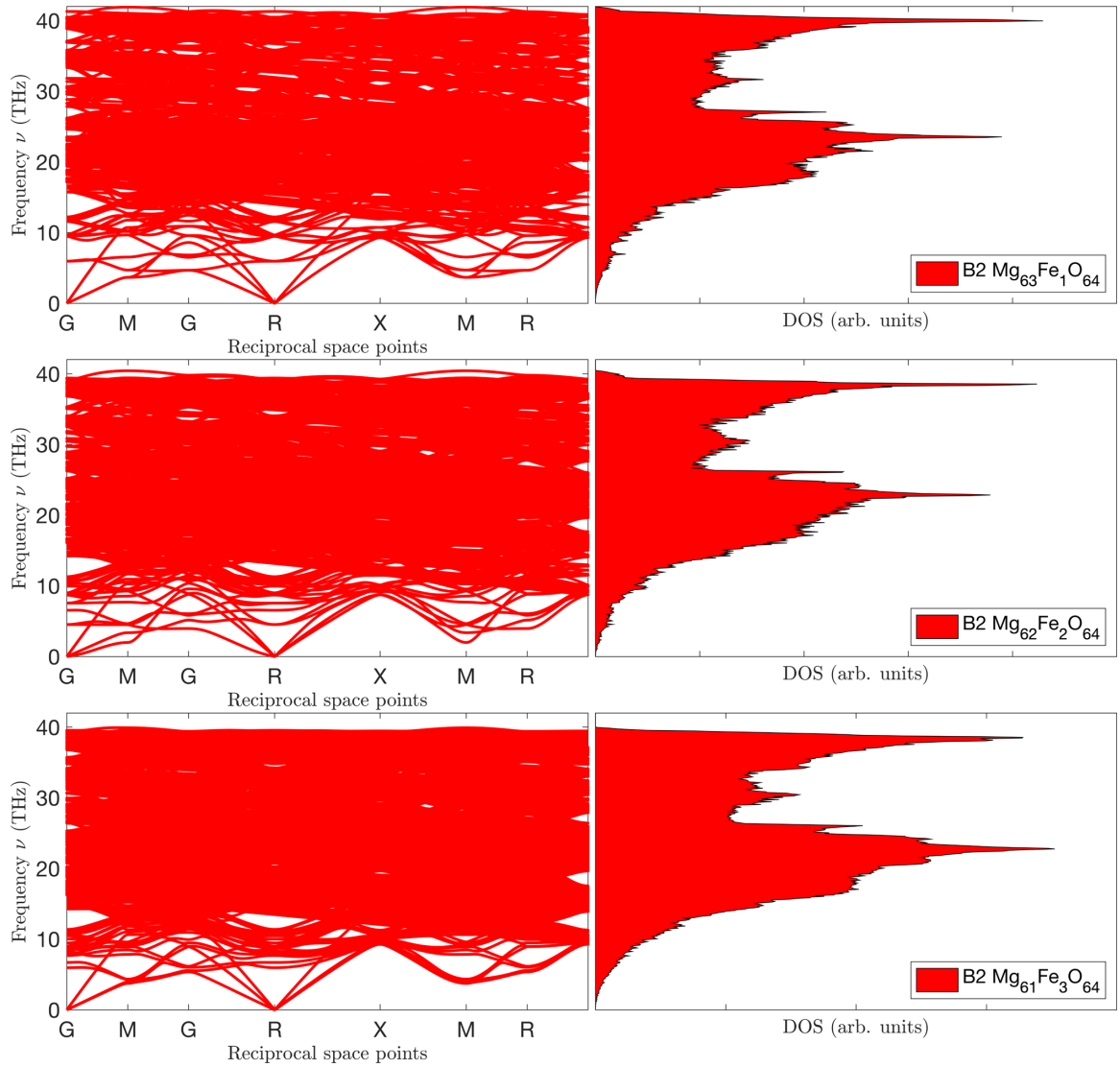

FIG. 5. Phonon dispersion of $Mg_{63}Fe_1O_{64}$, $Mg_{62}Fe_2O_{64}$, and $Mg_{61}Fe_3O_{64}$ in the $B2$ crystalline structure at ∼500 GPa.

domain of validity of the QHA has to be taken cautiously, particularly when looking at phase transitions where differences of a few meV [at 7000 K we find a variation of ∼60 meV for $G^{B1}(P)$, and ∼100 meV for $G^{B2}(P)$] in the Gibbs free energy can induce a difference of several GPa on the transition pressure (the correction is ∼15% at 7000 K).

B. Thermodynamics of ferropericlase

Our method successfully reproduces previous results on MgO phase transition. Moreover, using the phonon frequencies and the free energy of the system we computed thermodynamic properties such as specific heat at constant volume and the volume thermal expansion coefficient (reported in the Supplemental Material [17]), obtaining a good agreement with experimental results. Now we extended the previous study to the $Mg_xFe_{1-x}O$ ferropericlase.

The percentage of iron impurities in ferropericlase in the Earth's mantle is generally believed to be ∼5%-15%, however, we start with substituting just one Mg atom with an Fe atom in the 128 atoms supercell (corresponding to an iron impurities' percentage of ∼1.5%) and then progressively raise the number of Fe atoms, to show how MgO properties are gradually modified by the impurities in $Mg_{62}Fe_2O_{64}$ (c_{Fe} ∼ 3%) and $Mg_{61}Fe_3O_{64}$ (c_{Fe} ∼ 5%).

1. Vibrating lattice

Figures 4 and 5 show the phonon dispersion of $Mg_{63}Fe_1O_{64}$, $Mg_{62}Fe_2O_{64}$, and $Mg_{61}Fe_3O_{64}$ in the $B1$ and $B2$ crystalline structures at P ∼ 500 GPa. In both cases, increasing the number of impurities gradually reduces the highest frequency of the spectrum, with a more significant effect in the $B2$ structure.

It is important to mention that we found that the instability of the $B2$ phase persists at significant higher pressures compared to MgO (unstable below ∼110 GPa), in fact there are imaginary frequencies almost till ∼300 GPa. Marcondes *et al.* [13] recently studied the dynamical stability of $B1$ phase around the high-spin (HS) to low-spin (LS) transition, and found that there are no soft phonons modes across the HS-LS

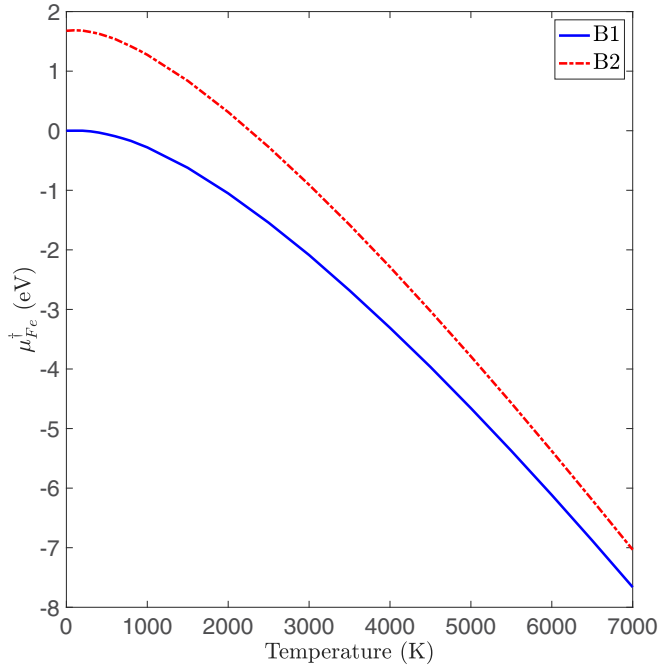

FIG. 6. Functions $\mu^{\dagger,B1}(P,T)$, $\mu^{\dagger,B2}(P,T)$ at $P = 400$ GPa. The curves are offset by $\mu^{\dagger,B1}$ in order to evidence the difference $\mu^{\dagger,B2} - \mu^{\dagger,B1}$.

crossover and for all pressures relevant for the Earth's mantle. Here we are mainly interested in the region of the $B1$-$B2$ transition pressure, where iron is LS, and so all our calculation have been performed without including spin polarization.

2. Repulsive Fe-Fe interactions

The contribution of the iron spatial distribution has been computed according to the procedure described in Sec. II E. Here we only report the main aspects of this calculation. More details can be found in the SM [17], together with a description of the effects of iron impurities on the volume thermal expansion coefficient.

First, we computed the free energy $F(V,T) = E(V) + F_{\rm harm}(V,T)$ for several ferropericlase configurations with two iron atoms in the 128 atoms supercell. If the impurities get very close to each other (first or second nearest neighbors), there is a repulsive interaction that is ∼0.2 eV in the $B1$ structure and ∼0.7 eV in the $B2$ one. This interaction becomes negligible when the two atoms are third nearest neighbors.

Adding one more iron atom, we find that three-body effects are almost negligible in the $B1$ structure, in fact the energy of a "clustered" configuration (three couples of first or second nearest neighbors) is ∼0.6 eV, i.e., is approximately given by the sum of the interaction energy of each couple (computed in previous case). Differently, the three-body effects seem to play a more important role in the $B2$ case, since the repulsive interaction of a clustered configuration (∼1.9 eV) is less than the sum of the couple interaction energy computed in the two impurities case.

However, first of all, clustered configurations are disadvantaged from the entropic weight, i.e., the number of configurations with first or second nearest neighbors Fe atoms are few if compared with the weight of all the other configurations. Moreover, since the energy gaps are $\sim 10^3$–10^4 K, these configurations are rarely visited along the Monte Carlo simulations, i.e., they give a small contribution (∼0.01–0.1 eV) to the free energy. This small contribution is almost equal in the two crystalline structures, therefore it barely affects the transition pressure.

3. B1-B2 phase transition

Once we have computed the Gibbs free energies $G(N_{\rm Mg}, N_{\rm Fe})$ for $N_{\rm Fe} = 0$ (pure MgO) and $N_{\rm Fe} = 1, 2, 3$, we used Eq. (16) to compute the chemical potentials $\bar{\mu}_{\rm Fe}(c_{\rm Fe})$ for $c_{\rm Fe} = 0.007, 0.015, 0.023$. Then we can fit Eq. (7) as a function of the concentration $c_{\rm Fe}$ and obtain the functions $\mu^{\dagger,i}$, λ^i for both crystalline structures. For instance, we report in Fig. 6 the chemical potentials $\mu^{\dagger,i}(P,T)$ in the $B1$ and $B2$ phases as a function of temperature, at $P = 400$ GPa. Analogously, Fig. 7 shows the functions $\mu^{\dagger,i}(P,T)$ [Fig. 7(a)] and $\lambda^i(P,T)$ [Fig. 7(b)] as functions of pressure at the fixed temperature $T = 3000$ K.

However, the term taking part in the evaluation of the exponential in Eq. (8) is the function $\lambda^i(P,T)$ multiplied by the correspondent concentration $c^i_{\rm Fe}$, which is in general different between the two phases. For this reason, in Fig. 7(c) we also show the functions $\lambda^i c^i_{\rm Fe}$ considering, for instance, an initial iron concentration of $c^{B1}_{\rm Fe} \sim 2\%$ and possible concentrations $c^{B2}_{\rm Fe}$ (fractions of $c^{B1}_{\rm Fe}$).

We find

$$\Delta\mu^{\dagger}_{B1,B2} = \mu^{\dagger,B2} - \mu^{\dagger,B1} \sim 1 \text{ eV}, \tag{32}$$

$$\Delta\lambda_{B1,B2} = \lambda^{B2} c^{B2}_{\rm Fe} - \lambda^{B1} c^{B1}_{\rm Fe} \sim [-0.5, 0.1] \text{ eV}. \tag{33}$$

This means that for small initial iron concentrations ($c^{B1}_{\rm Fe} < 5\%$), even in the extreme case of $c^{B2}_{\rm Fe} \to 0$, the term that controls the behavior of the phase boundary (and of the iron concentration between the two phases) is $\Delta\mu^{\dagger}_{B1,B2}$, which is independent of concentration. Therefore, we can compute the phase boundary also for concentrations slightly higher than $c^{B1}_{\rm Fe} = 0.023$, expecting to commit a small error due to a possible variation of $\Delta\lambda_{B1,B2}$. In particular, to check this approximation, we proceeded as follows: the accurate analysis of $Mg_{62}Fe_2O_{64}$ and $Mg_{61}Fe_3O_{64}$ showed that the excess free energy of mixing determines a very small correction to the transition pressure (almost 0.1 GPa at low temperatures and at most 1 GPa at $T \sim 7000$ K). For this reason, using the same technical parameters of the previous case, we computed the Gibbs free energy also for $Mg_{58}Fe_6O_{64}$, corresponding to an iron concentration of ∼10%. For simplicity we consider a partially clustered configuration of the six iron impurities, since it led to a higher symmetry structure and significantly reduces the number of displacements needed to compute the force constant matrix. According to the previous analysis, we expect to overestimate the transition pressure at most by ∼2-3 GPa, therefore it is a good compromise to explore almost completely the range of iron percentage that should characterize ferropericlase at planetary interior conditions. Once we have the Gibbs free energy $G^i(N_{\rm Mg} = 58, N_{\rm Fe} = 6)$, we can re-interpolate the chemical potential $\bar{\mu}^i_{\rm Fe}$ (as a function of the concentration) and carry out the *ab initio* functions $\mu^{\dagger,i}(P,T)$ and $\lambda^i(P,T)$. In particular, the new contribution

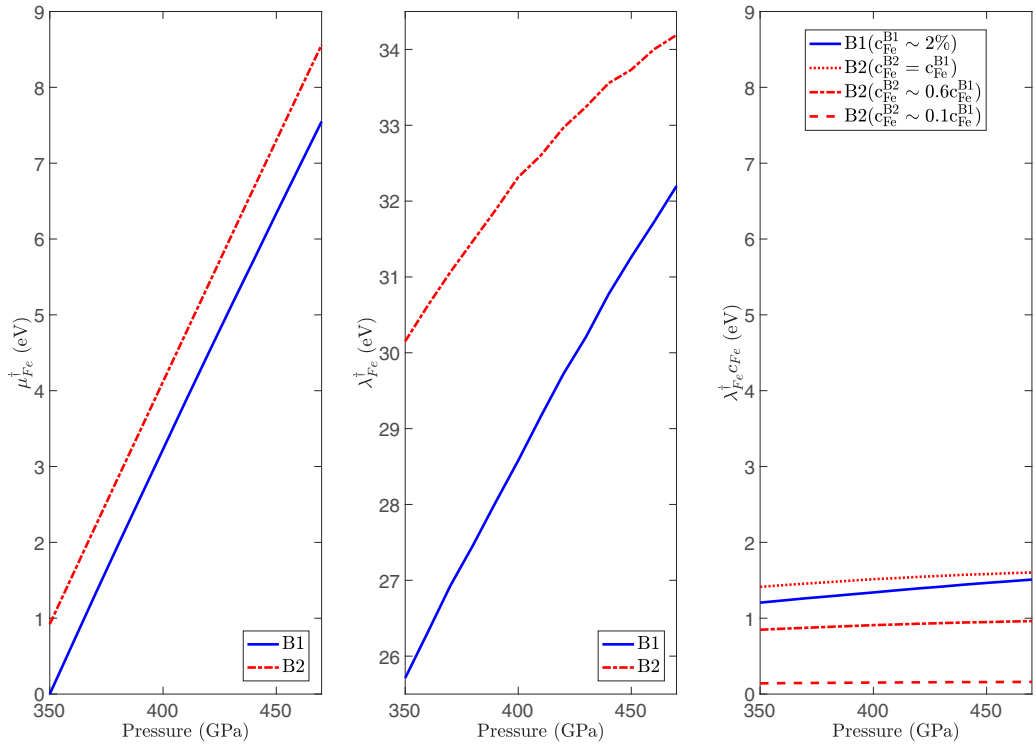

FIG. 7. Functions $\mu^{\dagger,B1}(P,T)$, $\mu^{\dagger,B2}(P,T)$ (a) and $\lambda^{B1}(P,T)$, $\lambda^{B2}(P,T)$ (b) at $T = 3000$ K. The curves $\mu^{\dagger}$ are offset by the minimum of $\mu^{\dagger,B1}$ in order to highlight the difference $\mu^{\dagger,B2} - \mu^{\dagger,B1}$. (c) Functions $\lambda^{B1}(P,T)c_{\mathrm{Fe}}^{B1}$, $\lambda^{B2}(P,T)c_{\mathrm{Fe}}^{B2}$, considering, for instance, an initial iron concentration of $c_{\mathrm{Fe}}^{B1} \sim 2\%$ and possible concentrations c_{Fe}^{B2} (fractions of c_{Fe}^{B1}). The plot is reported on the same scale of the functions $\mu^{\dagger}$, in order to compare the two terms taking part to the evaluation of the exponential in Eq. (8).

defines a slight correction to the linear behavior of $\bar{\mu}_{\mathrm{Fe}}$ in the $B1$ crystalline structure, with a 1% variation of the parameters $\mu^{\dagger}$, λ, while it is more important in the $B2$ phase (parameters' variation of ∼10%).

This approximation allowed us to solve Eqs. (6) and (13) simultaneously for an initial iron concentration of $c_{\mathrm{Fe}}^{B1} = 0.007, 0.015, 0.023, 0.031, 0.047$ (for several fixed pressures), obtaining the concentration ratio $c_{\mathrm{Fe}}^{B2}/c_{\mathrm{Fe}}^{B1}$ and the transition temperature associated with the beginning of the phase transition, i.e., the transition from the $B1$ structure to the $B1 + B2$ coexisting region.

In Fig. 8 we report the percentage ratio $c_{\mathrm{Fe}}^{B2}/c_{\mathrm{Fe}}^{B1}$, computed with an initial iron percentage $c_{\mathrm{Fe}}^{B1} = 0.007, 0.015, 0.031, 0.047$. It is clear that, according to our data, there is a nonhomogeneous distribution of the iron impurities among the phase transition: based on Eq. (32), we can observe that the chemical potential in the $B2$ crystalline structure is higher than the one in the $B1$ phase. This means that, in particular at low temperatures (high transition pressures), the exponential function in Eq. (8) is much greater than 1, and so $c_{\mathrm{Fe}}^{B1} \gg c_{\mathrm{Fe}}^{B2}$. The difference in the chemical potentials decreases with temperature, leading to an increase in the concentration of iron atoms flowing into the simple cubic structure. This effect becomes in particular more important as the iron concentration increases. As noted before, this analysis is valid only for small iron concentrations, where the difference $\Delta\lambda_{B1,B2}$ [Eq. (33)] plays a minor role compared to $\Delta\mu_{B1,B2}^{\dagger}$ [Eq. (32)].

Using the ratio $c_{\mathrm{Fe}}^{B2}/c_{\mathrm{Fe}}^{B1}$ we can compute the iron concentration in the $B2$ phase for all the transition pressures defining the limit between the $B1$ phase and the coexisting region, and yet obtain the transition curve corresponding to the limit between the $B1 + B2$ region and the $B2$ structure.

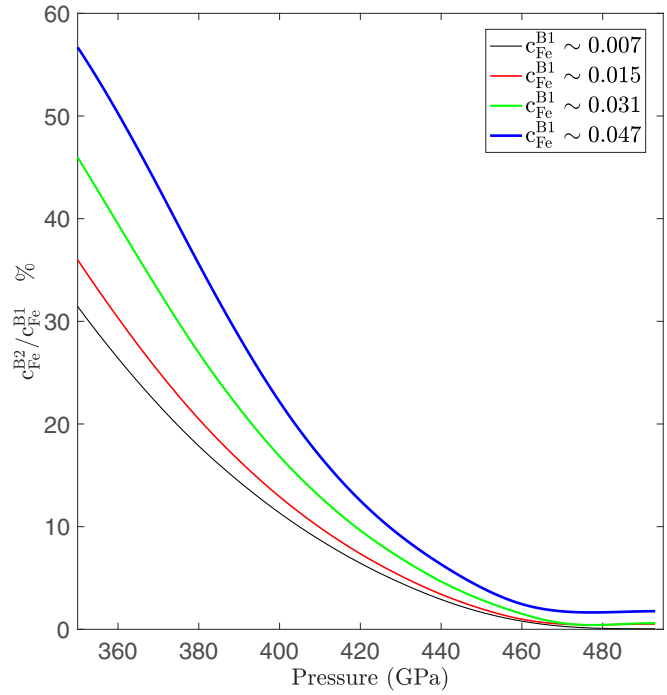

FIG. 8. Concentration of iron impurities in the $B2$ crystalline structure. On the y axis is reported the percentage ratio $c_{\mathrm{Fe}}^{B2}/c_{\mathrm{Fe}}^{B1}$.

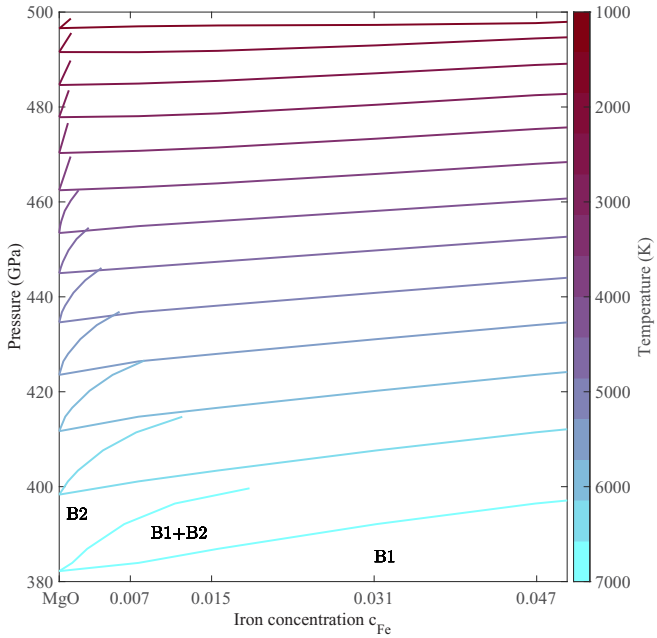

FIG. 9. Transition pressure of MgO periclase and $Mg_xFe_{1-x}O$ ferropericlase as a function of iron concentration for several fixed temperatures.

All the results are reported in Fig. 9. Increasing the number of iron substitutions defines a gradual rise in the transition pressure at fixed temperature, therefore the impurities contribute to improving the high-pressure stability of the $B1$ crystalline structure. The width of the coexisting region decreases in the high temperature limit, consistently with the more homogeneous distribution of the iron impurities and with the high temperature limit of Eq. (8).

Fixing the iron concentration and fitting the transition curve delimiting the $B1$ and $B2$ phases, we can finally reconstruct the phase diagram of $Mg_xFe_{1-x}O$ ferropericlase for a fixed iron percentage. However, we notice that due to the low temperature (high transition pressure) nonhomogeneous iron distribution between the two phases, we were able to reconstruct the transition line between the coexisting region and the $B2$ crystalline structure only for very low iron concentrations. In Fig. 10, in particular, we report the phase diagram for the lowest analyzed concentration, i.e., $c_{Fe} \sim 0.007$ and $c_{Fe} \sim 0.015$. The transition line between the coexisting region and the $B2$ structure is represented with a red thick band, defined by the error bars of the fit.

As a consequence of the linear approximation in Eq. (11), in the zero-temperature limit the equilibrium condition becomes independent on the iron concentration and simplifies in the equilibrium condition of pure MgO, explaining the loop closure and the zero-temperature value of the transition pressure. Above zero temperature, our data show that even a small concentration of iron increases the stability of the $B1$ structure.

Very recently, the $B1$-$B2$ phase transition of pure FeO and MgO has been experimentally investigated [14], and a pressure-concentration phase diagram relative to the phase transition in ferropericlase, at the fixed temperature of $T = 4000$ K, has been proposed in the approximation of an ideal mixing between the two end members, showing a decrease of the pure MgO transition pressure due to the introduction

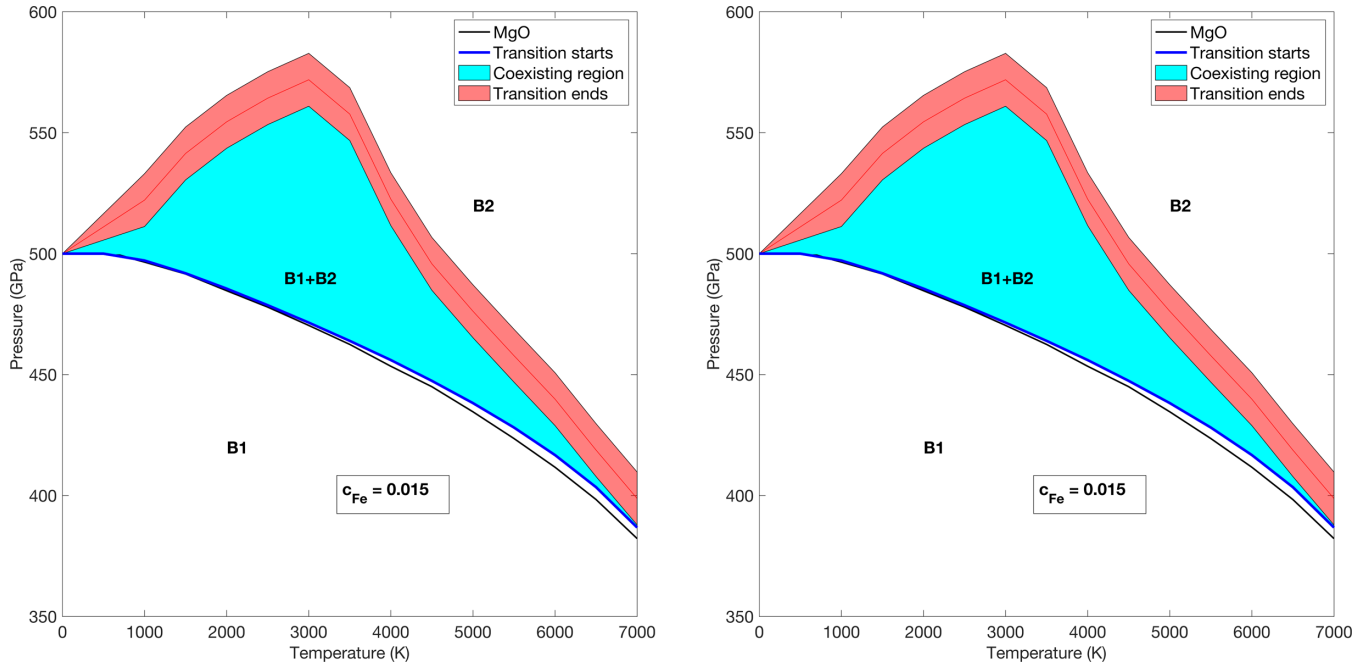

FIG. 10. Phase diagram of MgO periclase and $Mg_xFe_{1-x}O$ ferropericlase, with iron concentrations $c_{Fe} \sim 0.007, 0.015$. The transition line from the coexisting region to the $B2$ structure is represented with a red thick band, defined by the error bars. The large coexisting region is due to the strong partitioning of iron atoms in the $B1$ structure, caused by the relatively large difference between the iron *excess* chemical potentials in the two phases. The coexistence loop closes at high temperature, as iron begins to partitions more uniformly between the two phases, and also as $T \to 0$, where the effect of the presence of iron on the chemical potential of MgO vanishes [see Eq. (11)].

of iron impurities. Our result suggests that the ideal mixing approximation may not be accurate enough to reproduce the phase diagram in the limit of low impurities' concentration. However, since the $B1$-$B2$ transition pressure of FeO is lower than that of MgO, we believe that the increase of the transition pressure with increasing iron concentration should change for iron concentrations higher than the ones explored in our work. Moreover, while this paper was in submission, a new theoretical study of the $B1$-$B2$ phase transition in ferropericlase was published on the arXiv [15], reporting the phase diagram of ferropericlase, in the temperature range from 3000 to 8000 K, and for a concentration $c_{\mathrm{Fe}} = 0.1$, which is higher than the ones considered in our work. The results are qualitatively in agreement in predicting an increase of the $B1$ to $B2$ transition pressure due to the presence of iron impurities and a decrease of the coexisting region width in the high-temperature limit, even though the coexisting region width is larger for the small concentration considered in our work. However, as noted before, including simulations with higher impurities concentration could significantly influence the phase diagram in Fig. 9, therefore our data do not allow an accurate prediction on the phase diagram for concentrations significantly higher than the ones we have considered.

Limited by our computational resources we did not compute the anharmonic effects for ferropericlase, and for this reason we only report the comparison between the ferropericlase phase boundary and the periclase quasiharmonic one. A complete analysis certainly requires further investigation in the future. However, considering the effects of the anharmonic contribution in the MgO, we reasonably expect this term only to raise the transition pressure in the high-temperature region, without influencing the general trend of the phase diagram obtained in the QHA limit.

IV. CONCLUSIONS

We have developed a high-accuracy method to analyze the crystal structure and the thermodynamic stability of materials at planetary interior conditions. Furthermore, we provided a technique to include the configurational contribution to the free energy due to the possible spatial distribution of substitutional alloys in a solid.

In detail, we used this method to study the phase transition between the $B1$ and the $B2$ crystalline structures in periclase and ferropericlase.

High-accuracy results, which include anharmonic effects in the computation of the vibrational free energy, are carried out only for MgO, therefore further simulations are needed to obtain a complete comparison between the two different materials.

We showed how the increasing number of iron impurities gradually determines an increase in the transition pressure at a fixed temperature, i.e., the iron impurities contribute to improving the structural and thermodynamic stability of the low-pressure structure. Therefore, according to our results, the presence of iron atoms confirms that the phase transition does not occur in the Earth's mantle. However, it can still happen in high-density super-Earths, where the pressure can reach values up to the TPa. According to our data, there is a significant low temperature nonhomogeneous distribution of the Fe atoms among the phase transition, which is due to the higher nonconfigurational part of the chemical potential of Fe in the $B2$ crystalline structure. The increase of the chemical potential in the $B2$ phase perhaps could be ascribed to geometrical differences between the two structures, or to a different electron transfer between the iron atom and the oxygen around it. Increasing both the temperature and the initial iron concentration lead to a more homogeneous distribution of the impurities between the two phases. This allows us to describe the phase diagram of ferropericlase only for the small iron concentrations considered in our simulations, and further investigation is certainly necessary in order to extend this analysis to concentrations relevant to the Earth's and super-Earths' mantle.

ACKNOWLEDGMENTS

The simulations have been performed on the cluster `NANOMAT` of University Federico II of Naples, working on average with 6 quad-core CPUs (2.80GHz − 12Gb per CPU). The authors would like to thank Giovanni Cantele for the use of `NANOMAT` and for support. Calculations were also performed on the Cambridge Service for Data Driven Discovery (CSD3) operated by the University of Cambridge Research Computing Service [32] provided by Dell EMC and Intel using Tier-2 funding from the Engineering and Physical Sciences Research Council (capital Grant No. EP/P020259/1), and DiRAC funding from the Science and Technology Facilities Council [33].

[1] T. Duffy, N. Madhusudhan, and K. K. M. Lee, *2.07-Mineralogy of Super-Earth Planets*, Treatise on Geophysics (Elsevier, Amsterdam, 2015), pp. 149–178

[2] M. J. Mehl, R. E. Cohen, and H. Krakauer, J. Geophys. Res. **93**, 8009 (1988).

[3] D. Valencia, D. D. Sasselov, and R. J. O'Connell, Icarus **181**, 545 (2006).

[4] N. Nettelmann, B. Holst, A. Kietzmann, M. French, R. Redmer, and D. Blaschke, Astrophys. J. **683**, 1217 (2008).

[5] A. Metsue and T. Tsuchiya, Geophys. J. Int. **190**, 310 (2012).

[6] F. Coppari, R. F. Smith, J. H. Eggert, J. Wang, J. R. Rygg, A. Lazicki, J. A. Hawreliak, G. W. Collins, and T. S. Dufft, Nat. Geosci. **6**, 926 (2013).

[7] R. S. McWilliams, D. K. Spaulding, J. H. Eggert, P. M. Celliers, D. G Hicks, R. F. Smith, G. W. Collins, and R. Jeanloz, Science **338**, 1330 (2012).

[8] R. M. Bolis, G. Morard, T. Vinci, A. Ravasio, M. Guarguaglini E. Bambrink, M. Koenig, R. Musella, F. Remus, J. Bouchet, N. Ozaki, K. Miyanashi, T. Sekine, Y. Sakawa, T. Sano, F. Guyot, R. Kodama, and A. Benuzzi-Mounaix, Geophys. Res. Lett. **43**, 9475 (2016).

[9] S. Root, L. Shulenburger, R. W. Lemke, D. H. Dolan, T. R. Mattsson, and M. P. Desjarlais, Phys. Rev. Lett. **115**, 198501 (2015).
[10] K. Miyanishi, Y. Tange, N. Ozaki, T. Kimura, T. Sano, Y. Sakawa, T. Tsuchiya, and R. Kodama, Phys. Rev. E **92**, 023103 (2015).
[11] J. Bouchet, F. Bottin, V. Recoules, F. Remus, G. Morard, R. M. Bolis, and A. Benuzzi-Mounaix, Phys. Rev. B **99**, 094113 (2019).
[12] S.-i. Karato, Icarus **212**, 14 (2011).
[13] M. L. Marcondes, F. Zheng, and R. M. Wentzcovitch, Phys. Rev. B **102**, 104112 (2020).
[14] F. Coppari, R. F. Smith, J. Wang, M. Millot, D. Kim, J. R. Rygg, S. Hamel, J. H. Eggert, and T. S. Duffy, Nat. Geosci. **14**, 121 (2021).
[15] T. Wan, Y. Sun, and R. M. Wentzcovitch, Intermediate spin state and the *B*1-*B*2 transition in ferropericlase, Phys. Rev. Research **4**, 023078 (2022).
[16] H. Hsu and K. Umemoto, arXiv:2011.07737.
[17] See Supplemental Material at http://link.aps.org/supplemental/10.1103/PhysRevB.105.134109 for the computation of thermodynamic properties (specific heat at constant volume and volume thermal expansion) of periclase and ferropericlase, and for the details on the repulsive Fe-Fe interactions.
[18] D. Alfè, M. J. Gillan, and G. D. Price, J. Chem. Phys. **116**, 7127 (2002).
[19] G. Kresse and J. Fürthmuller, Phys. Rev. B **54**, 11169 (1996).
[20] G. Kresse and D. Joubert, Phys. Rev. B **59**, 1758 (1999).
[21] J. P. Perdew, K. Burke, and M. Ernzerhof, Phys. Rev. Lett. **77**, 3865 (1996).
[22] H. J. Monkhorst and J. D. Pack, Phys. Rev. B **13**, 5188 (1976).
[23] F. Birch, Phys. Rev. **71**, 809 (1947).
[24] D. Alfè, Comput. Phys. Commun. **180**, 2622 (2009).
[25] D. Frenkel and B. Smit, *Understanding Molecular Simulation*, 2nd ed. (Academic, New York, 2001).
[26] H. C. Andersen, J. Chem. Phys. **72**, 2384 (1980).
[27] A. R. Oganov, M. J. Gillan, and G. D. Price, J. Chem. Phys. **118**, 10174 (2003).
[28] B. B. Karki, R. M. Wentzcovitch, S. de Gironcoli, and S. Baroni, Phys. Rev. B **61**, 8793 (2000).
[29] S. Speziale, C.-S. Zha, T. S. Duffy, R. J. Hemley, and H. K. Mao, J. Geophys. Res. **106**, 515 (2001).
[30] M. J. L. Sangsters, G. Peckham, and D. H. Saunderson, J. Phys. C: Solid State Phys. **3**, 1026 (1970).
[31] J. R. Jasperse, A. Kahan, J. N. Plendl, and S. S. Mitra, Phys. Rev. **146**, 526 (1966).
[32] www.csd3.cam.ac.uk.
[33] www.dirac.ac.uk.